Title	Model calculation of Cr dissolution behavior of ODS ferritic steel in high-temperature flowing sodium environment
Author(s)	Otsuka Satoshi, Tanno Takashi, Oka Hiroshi, Yano Yasuhide, Kato Shoichi, Furukawa Tomohiro, Kaito Takeji
Citation	Journal of Nuclear Materials,505,p.44-53
Text Version	Accepted Manuscript
URL	https://jopss.jaea.go.jp/search/servlet/search?5061506
DOI	https://doi.org/10.1016/j.jnucmat.2018.03.054
Right	© 2018. This manuscript version is made available under the CC-BY-NC-ND 4.0 license http://creativecommons.org/licenses/by-nc-nd/4.0/

- Title: Model calculation of Cr dissolution behavior of ODS ferritic steel in high-temperature flowing sodium environment

- Authors : Satoshi Ohtsuka*, Takashi Tanno, Hiroshi Oka, Yasuhide Yano, Shoichi Kato, Tomohiro Furukawa, Takeji Kaito

Japan Atomic Energy Agency, 4002 Narita-cho, Oarai-machi, Ibaraki 311-1393, Japan

* Corresponding author:
Satoshi Ohtsuka
Japan Atomic Energy Agency, 4002 Narita-cho, Oarai-machi, Ibaraki 311-1393, Japan
E-mail address: ohtsuka.satoshi@jaea.go.jp
Tel : +81-29-267-1919
Fax : +81-29-267-1676

[Highlights]

- A calculation model was constructed to systematically study the Cr dissolution behavior of fuel cladding tube.
- Chromium dissolution was significantly influenced by small changes in Cr concentration (i.e. chemical potential of Cr) in liquid sodium in the model calculation.
- Both the experimental measurement and the model calculation indicated that the cladding surface Cr concentrations in 9Cr- and 12Cr-ODS steels converged approximately to a unique value.

[Abstract]

A calculation model was constructed to systematically study the effects of environmental conditions (i.e. Cr concentration in sodium, test temperature, axial temperature gradient of fuel pin, and sodium flow velocity) on Cr dissolution behavior. Chromium dissolution was largely influenced by small changes in Cr concentration (i.e. chemical potential of Cr) in liquid sodium in the model calculation. Chromium concentration in sodium coolant, therefore, should be recognized as a critical parameter for the prediction and management of Cr dissolution behavior in the sodium-cooled fast reactor (SFR) core. Because the fuel column length showed no impact on dissolution behavior in the model calculation, no significant downstream effects possibly take place in the SFR fuel cladding tube due to the much shorter length compared with sodium loops in the SFR plant and the large axial temperature gradient. The calculated profile of Cr concentration along the wall-thickness direction was consistent with that measured in BOR-60 irradiation test where Cr concentration in inlet sodium bulk flow was set at 0.07 wt ppm in the calculation.

[Keywords] Oxide dispersion strengthened steel, Fuel cladding tube, Sodium-cooled fast reactor, Cr dissolution, Flowing sodium

1. Introduction

Oxide dispersion strengthened (ODS) ferritic steel is recognized as high-strength and radiation-tolerant steel used for fast reactor fuel cladding tubes, fusion reactor material and accident tolerant fuel cladding tubes for light water reactors [1-12]. The Japan Atomic Energy Agency (JAEA) has been developing 9Cr- and 12Cr-ODS steels for the high burnup fuel cladding tubes of sodium-cooled fast reactors (SFR), which will be used up to 250 GWd/t (peak burnup) up to 700 ºC (hot spot mid-wall temperature) for enhancement of SFR economy. Research and development efforts on ODS steels for SFR cladding application include manufacturing and joining technology as well as the evaluation of out-of-piles mechanical properties and environmental effects such as neutron irradiation and sodium corrosion [1-4]. Among them, the evaluation of sodium environmental effects is important from the viewpoint of the in-reactor integrity evaluation of fuel elements since the outer surface of SFR fuel cladding tubes are exposed to high-temperature flowing sodium and the tube wall is very thin.

It has been reported that, when steels are used in high-temperature sodium, the solubility of steel constituent elements is increased in sodium [13], thus enhancing mass transfer phenomena such as dissolution, deposition and diffusion penetration of the solute elements [14-20]. Some studies have experimentally evaluated the mass transfer behavior of ODS steels in high-temperature sodium, e.g. out-of-piles stagnant sodium corrosion test (flow velocity < 0.001 m/sec) of 9-14Cr-ODS steels at 650-700 ºC [14, 16], out-of-piles flowing sodium loop corrosion test of 13, 14Cr-ODS steels at 600-700 ºC [14, 16], and fuel pin irradiation test of 9Cr- and 12Cr-ODS steels at a Russian experimental fast reactor BOR-60 [15]. These tests indicated the occurrence of Cr dissolution and Ni penetration in ODS steels, which were enhanced by the presence of sodium flow and elevating test temperature.

The driving force of the mechanism of mass transfer should be a gap of chemical potentials of solute elements in liquid sodium and cladding tube, in which solute elements diffuse along the gradient of chemical potentials from higher to lower potential parts. The chemical potential of Cr is dependent not only on temperature but also on impurity Cr concentration in sodium. For SFR fuel pins, therefore, in addition to typical parameters such as the test temperature, axial temperature gradient of fuel pin, and flow velocity [13-20], there may be effects on Cr dissolution behavior brought by impurity Cr concentration in sodium.

It is important to study the effects of these parameters on the mass transfer behavior for prediction in actual SFR fuel pins using limited experimental data. It would be a challenge to systematically obtain experimental data for the study of the effects of these parameters. Obtaining the data requires the preparation of elaborate test equipment and the derivation of many data. The fuel pin irradiation test is a key technique for demonstrating the irradiation performance of advanced fuel cladding tubes. It can provide flowing sodium corrosion data as well as various important data such as fuel-cladding chemical interaction (FCCI) and irradiation-induced deformation. However, the derivation of systematic sodium corrosion data is impossible only by fuel pin irradiation test. The purpose of this study is to systematically and numerically evaluate the effects of important parameters (i.e. Cr concentration in sodium, test temperature, axial temperature gradient of fuel pin and sodium flow velocity) on Cr dissolution behavior using model calculation. The model calculation offers important results conducive to the effective planning of sodium corrosion test and discussions on extrapolation from limited experimental data. This paper also shows Cr dissolution data for both 9Cr- and 12Cr-ODS steel cladding tubes irradiated in BOR-60[15], which were compared with the model calculation results, and the validity of model calculation was discussed.

2. Procedure

2.1 BOR-60 fuel pin irradiation [15]

A series of fuel pin irradiation tests of 9Cr- and 12Cr-ODS steel cladding tubes was carried out at the Russian experimental fast reactor BOR-60 [15]. The fuel pin irradiation test included three tests. This paper indicates the result of the second test, in which cross-sectional Cr concentration distributions (i.e., data on Cr dissolution behavior) were measured both for 9Cr- and 12Cr-ODS steel cladding tubes at high-temperature axial positions. The second test achieved a maximum burnup of 10.5 at% and a peak neutron dose of 45 dpa; the test durations were 13,570 h and the time-averaged irradiation temperatures calculated ranged from 320 ^{o}C to 670 ^{o}C, respectively, at the bottom and top of the fuel column. The sodium flow velocity in experimental fuel assemblies (EFAs) was approximately 2 m/sec. The basic chemical compositions of 9Cr- and 12Cr-ODS steels were Fe-0.13wt%C-9Cr-2W-0.2Ti-0.35Y_2O_3 and Fe-0.03wt%C-12Cr-2W-0.27Ti-0.23Y_2O_3, respectively. The size of ODS steel cladding tubes was 6.9 mm in diameter and 0.4 mm in wall thickness. The fuel column length was 300 mm for 9Cr-ODS steel pins, and 450 mm for 12Cr-ODS steel pins [15]. After the irradiation, the transverse section at the top of fuel column was observed using a scanning electron microscope (SEM; FEI/Philips XL30 ESEM-TMP) at the hot laboratory of Research Institute of Atomic Reactors (RIAR). The semi-quantitative line analyses of Cr concentration were carried out using wavelength dispersive X-ray spectroscopy (WDX; Oxford INCA Wave 700). The WDX line analysis data on 9Cr-ODS steel were reported previously [15] while new data on 12Cr-ODS steel are reported in this paper.

2.2 Model calculation

2.2.1 Modelling

The Cr dissolution from cladding tube to liquid sodium is thought to take place since the chemical potential of Cr in liquid sodium is lower than that in cladding tubes. The outline of Cr dissolution process modelled in this study is described below:

(a) As schematically shown in Figure 1, to maintain continuity in the chemical potential of Cr at the cladding-liquid sodium interface, Cr concentration on the cladding surface declines to a level at which the chemical potentials of Cr at the cladding side and the liquid sodium side of interface are equal.
(b) To maintain the mass balance, the Cr flux at cladding surface (J1(2)) corresponds with that in liquid sodium at the interface (J2), as schematically shown in Figure 1. This model assumes no change in the cladding wall thickness. In the BOR-60 fuel pin irradiation test, Cr dissolution took place in 9Cr- and 12Cr-ODS steel cladding tubes while no significant recession of tube wall thickness was observed [15].
(c) The boundary condition adopted in this model calculation is that the Cr concentration at the cladding tube surface satisfies the two requirements, (a) and (b). With this surface Cr concentration as the boundary condition, Cr diffusion in radial direction progresses, thereby causing Cr dissolution into liquid sodium.

An R-Z two dimensional system was adopted in the calculation, as shown in Figure 2. Mesh partitioning on the Z-axis was performed with even intervals while that on the R-axis by the following equation to provide smaller intervals near the cladding surface:

$$R(1)=0,\ \ R(M)= WT \times A^{(M-N_R)} \quad (M=2\sim N_R) \tag{1}$$

where M represents a positive integer, R(M) is the distance from the cladding surface on the R-axis, WT is the wall thickness of a cladding tube, N_R is the number of partitioned meshes on the R-axis. This type of mesh partitioning was chosen for improvement of calculation accuracy in the Cr flux at the cladding surface. In this study, a value of 1.5 was adopted for parameter A. Figure 3 shows a cross-sectional view of the calculation system. Considering the system symmetry, the Cr flux through the peripheral length of a and b and the height of partitioned mesh in Z-direction was calculated to increase the average Cr concentration of bulk sodium flow with the volume having the area of S and the height of partitioned mesh.

Figure 4 shows the flow chart for the calculation. The Cr dissolution calculations were conducted in order from the bottom (sodium inlet) to the top row meshes (sodium outlet). In each row, the surface Cr concentration of cladding tube was calculated under the two requirements, i.e. continuity of Cr chemical potential at the interface (2.2.1(a)) and Cr mass balance at the interface (2.2.1(b)). The details on the calculation of 2.2.1(a) are described in

2.2.2. For time increment (Δt), one-dimensional diffusion calculations were executed with an approximation to maintain the surface Cr concentration (C(1)) at a constant for Δt, thereby evaluating the change of Cr concentration profiles in the R-direction after Δt. The following time increment (Δt) was adopted in this calculation.

$$\Delta \mathrm{t} = \frac{L}{N_Z \times V_{Na}} \tag{2}$$

where L represents the total length for the calculation area on Z axis (Figure 2), N_Z is the number of partitioned meshes on the Z-axis, V_{Na} is the bulk flow velocity of liquid sodium. As shown in Figure 5, one-dimensional diffusion calculations were performed using the following equations.

$$\mathrm{C(M)}|_{\mathrm{t=t0+\Delta t}} = \mathrm{C(M)}|_{\mathrm{t=t0}} + \frac{\mathrm{J1(M+1)-J1(M)}}{\mathrm{DR(M)}} \cdot \Delta \mathrm{t} \quad (\mathrm{M}=2\sim \mathrm{N_R}) \tag{3}$$

$$\mathrm{J1(M)} = \mathrm{D_{Cr}} \cdot \frac{\mathrm{C(M)-C(M-1)}}{\mathrm{R(M)-R(M-1)}} \quad (\mathrm{M}=2\sim \mathrm{N_R}) \tag{4}$$

$$DR(1) = \frac{R(1)}{2} \tag{5}$$

$$\mathrm{DR(M)} = \frac{\mathrm{R(M+1)-R(M-1)}}{2} \quad (\mathrm{M}=2\sim \mathrm{N_R}) \tag{6}$$

where C(M) represents the Cr concentration at the R-axis position R(M), D_{Cr} is the diffusion coefficient of Cr in cladding tube, J1(M) is the Cr flux in R-direction at a mesh between R-axis positions R(M) and R(M-1). The Cr flux at cladding surface (J1(2)) was calculated using the following equation.

$$\mathrm{J1(2)} = \mathrm{D_{Cr}} \cdot \frac{\mathrm{C(2)-C(1)}}{\mathrm{R(2)-R(1)}} \tag{7}$$

For incorporation of downstream effects into the model calculation, the amounts of Cr dissolution from cladding tube into liquid sodium were calculated using equation (7) for Δt, then included in the evaluation of the average Cr concentration in bulk sodium flow in the next upper mesh. As fresh liquid sodium was thought to come into fuel assemblies after passing through cold-traps, Cr concentration in the liquid sodium, which is in contact with the bottom mesh of the Z axis, was constantly maintained at an initial input concentration throughout the calculation. Since there are currently no data on the removal performance of impurity Cr in cold-traps, justification of this precondition is a subject for future discussion from the viewpoint of calculation accuracy and reliability.

A series of calculation, as displayed in Figure 4, is executed in the pre-determined cycles, which produces calculation results at a target simulation time. In this iteration calculation, cladding surface Cr concentration (C(1)) satisfying the boundary condition (Figure 1) and Cr concentration profiles along R-direction were calculated in order from the bottom to the top row meshes in every calculation cycle (Cy). Thus, this calculation provides the change of Cr concentration along R-direction for every time increment (Δt). Here, one cycle calculation means the sequential calculations from the bottom to the top row meshes (Figure 2). The calculation cycles (C) for the target simulation time (t_s) can be evaluated by the equation that follows..

$$t_s = \Delta t \times C = \frac{L \times C}{N_Z \times V_{Na}} \tag{8}$$

The Cr mass balance at the interface (2.2.1(b)) was calculated as described below. The Cr flux at the liquid sodium side of interface (J2) is expressed as:

$$J2 = kc \times (C(1)' - C(0)') \tag{9}$$

where kc represents the mass transfer coefficient of Cr in the boundary layer, C(1)' is Cr concentration at the liquid sodium side of interface, C(0)' is the average Cr concentration in bulk sodium flow as indicated in Figure 5. In the calculation, the following correlation was set to be maintained throughout the calculation.

$$J1(2) = J2 \tag{10}$$

In the fully developed turbulent flow, the solute concentration profile in flowing liquid is thought to be as is schematically shown in Figure 1, where the solute concentration linearly changes in the boundary layer, and is uniform in the bulk flow [13, 18, 20]. The mass transfer coefficient kc in the boundary layer is defined by:

$$kc = {D'_i}/{\delta} \tag{11}$$

where D'_i represents the diffusion coefficient of solute element i in the liquid, and δ is the thickness of the boundary layer. δ was expressed by:

$$\delta = \frac{d}{0.0165} \cdot \left(\frac{d \cdot U}{\nu}\right)^{-0.86} \cdot \left(\frac{\nu}{D'_i}\right)^{-0.33} \tag{12}$$

where d represents the hydraulic diameter (Figure 3), U is the bulk flow velocity, and ν is the kinematic viscosity of flowing liquid. This equation was derived from the basic equations in the fields of fluid mechanics, as described in Appendix. This equation shows that increasing the bulk flow velocity (U) thins the boundary layer, and thus increases the value of the mass transfer coefficient (equation (11)). That is, these equations show that increasing the bulk flow velocity promotes corrosion. Equations (11) and (12) were used in this calculation to take the flow velocity effects into consideration.

2.2.2 Equilibrium Cr concentrations at the cladding-liquid sodium interface

Using the general thermo-dynamic data, new correlations were formulated for calculation of

Cr concentrations at both the cladding side and liquid sodium side of the interface, where the Cr chemical potentials correspond with each other at both sides of the interface. In the liquid sodium, the Cr chemical potential (μ_{Cr}^{L}) was correlated with the mole fraction of solute Cr (x_{Cr}^{L}) by the general equation [21],

$$\mu_{Cr}^{L} = G_{Cr}^{0L} + \Omega_{Na-Cr}^{L} \cdot (1 - x_{Cr}^{L})^2 + RT \ln x_{Cr}^{L} \tag{13}$$

Likewise, the following equation was adopted as the correlation between the Cr chemical potential (μ_{Cr}^{BCC}) and the mole fraction of solute Cr (x_{Cr}^{BCC}) in the body-centered-cubic (BCC) matrix.

$$\mu_{Cr}^{BCC} = G_{Cr}^{0BCC} + \Omega_{Fe-Cr}^{BCC} \cdot (1 - x_{Cr}^{BCC})^2 + RT \ln x_{Cr}^{BCC} \tag{14}$$

where Ω_{Na-Cr}^{L} and Ω_{Fe-Cr}^{BCC} represent the interaction parameters of Na-Cr system in liquid, and Fe-Cr system in BCC matrix, respectively. G_{Cr}^{0L} and G_{Cr}^{0BCC} are the Gibbs free energies of pure liquid Cr and pure BCC-Cr, respectively. R and T are molar gas constant and temperature, respectively. The values of G_{Cr}^{0L} and G_{Cr}^{0BCC} are indicated elsewhere [e.g. 22]. J. O Anderson and Bo Sundman optimized the value of Ω_{Fe-Cr}^{BCC} for phase diagram calculations using the CALPHAD methods as [23]

$$\Omega_{Fe-Cr}^{BCC} = 20500 - 9.68 \times T \tag{15}$$

This equation was adopted for the current study. On the other hand, there are no reports evaluating the value of Ω_{Na-Cr}^{L}. Then, Ω_{Na-Cr}^{L} was approximately assessed in this study from equation (13) and Cr solubility data in liquid sodium [13, 24]. In the case that Cr is precipitated in the form of BCC-Cr in liquid sodium, equation (13) can be converted to the following equation,

$$\Omega_{Na-Cr}^{L} = \left(G_{Cr}^{0BCC} - G_{Cr}^{0L} - RT \ln x_{Cr}^{(s)}\right) / (1 - x_{Cr}^{(s)})^2 \tag{16}$$

where $x_{Cr}^{(s)}$ represents the solubility limit of Cr in liquid sodium. By substituting the reported equations of G_{Cr}^{0BCC}, G_{Cr}^{0L} [22], and the solubility limit of Cr in liquid sodium as a function of temperature [13, 24] into equation (16), the equation for Ω_{Na-Cr}^{L} was derived as follows:

$$\Omega_{Na-Cr}^{L} = 148.16 - 45.94 \times T \tag{17}$$

Figure 6 shows the Cr solubility line in liquid sodium obtained by the phase equilibrium calculation using the FactSage code [25]. In the calculation, equation (17) was used as Ω_{Na-Cr}^{L}, and Na-Cr solute liquid phase and BCC-Cr phase were included. The calculated Cr solubility line agrees well with experimental data. The combination of equations (13) and (14) provided the calculated Cr concentrations in BCC Fe-Cr and Liquid Na-Cr, where the Cr chemical potentials in both phases are identical, i.e. $\mu_{Cr}^{L} = \mu_{Cr}^{BCC}$. The examples of calculated Cr concentrations are shown in Figure 7, which indicates that the equilibrium Cr concentration in BCC Fe-Cr increases with Cr concentration in liquid sodium. It also indicates that the equilibrium Cr concentration in BCC Fe-Cr declines with an increase in temperature. This trend was caused by increased Cr solubility (i.e. decreasing Cr chemical potential) in liquid sodium with an increase in temperature. In the calculation, the equilibrium correlation (Figure 7) was invariably maintained at the interface. This calculation focused on the simulation of Cr dissolution behavior at high temperatures, and did not include the phenomena of deposition and diffusion penetration.

2.2.3 Input parameters

This calculation substituted the self-diffusion coefficient of liquid sodium (Table 1) evaluated at temperatures from 103 to 284 °C [26] for the diffusion coefficient of Cr in liquid sodium (D_{Cr}') by extrapolation. In this case, the Cr diffusion coefficients in liquid sodium were calculated as 1.6 x 10^{-8} m^2/sec at 400°C and 2.7x 10^{-8} m^2/sec at 700°C. As shown in equations (11) and (12), selection of D_{Cr}' influences the calculation of mass transfer coefficient, which is a dominant parameter in the calculation of flow velocity effects on Cr dissolution. Therefore, uncertainty of D_{Cr}' influences the quantitative reliability of calculated flow velocity effects such as critical flow velocity for saturation.

Figure 8 shows the diffusion coefficients of Cr and Ni in BCC-Fe [27] along with the diffusion coefficient of Ni in ODS steel [14]. As seen in Figure 8, the diffusion coefficient of Ni in ODS steel is apparently higher than that in BCC-Fe while those of Cr and Ni in BCC-Fe are roughly identical to each other. Since there is no data reported for the diffusion coefficient of Cr in ODS steel, the diffusion coefficient of Cr was substituted by that of Ni in ODS steel for this calculation. Table 2 shows the physical properties of liquid sodium [28] used for this calculation. Two types of binary systems were assumed for chemical compositions of cladding tubes: Fe-9wt%Cr and Fe-12wt%Cr. In the calculation, temperature was set at 300 °C at the bottom mesh and linearly increased along the z-axis to 700 °C at the top mesh. To study the effects of the fuel column length where temperature linearly increases, two lengths were assumed in the calculation: 0.3 m and 1.0 m (Figure 9). For simplicity, no temperature gradient along the R-direction (wall thickness direction) was assumed. The chromium concentration in liquid sodium at the bottom mesh (i.e. Cr concentration in the inlet sodium coolant ($C_{Cr}^{inletNa}$)) was set between 0.01 and 1 wt ppm. There is no information on management criteria of Cr concentration in liquid sodium coolant at BOR-60. As for the Japanese Experimental Fast Reactor Joyo (Mk-II core), the upper limit of Cr concentration is 5 wt ppm in liquid sodium coolant [29]. The flow velocity of liquid sodium coolant was set between 0.01 and 20 m/sec for the calculation.

3. Results and discussions

3.1 BOR-60 fuel pin irradiation test [15]

Figure 10 shows the WDX line analysis results of 9Cr- and 12Cr-ODS steel cladding tubes at the top of fuel column after the second irradiation test at BOR-60. It can be seen that the surface Cr dissolution took place both in 9Cr- and 12Cr-ODS steel cladding tubes. The Cr concentrations at the surface of cladding tube converged to approximately 5 wt% both in 9Cr- and 12Cr-ODS steels. Some observed peaks were caused by Cr carbide precipitations. The thickness of Cr dissolution layer in both steels were roughly equal to each other.

3.2 Calculation of flow velocity effects

Figure 11 shows the surface Cr concentration calculated as a function of the bulk flow velocity; the value for $C_{Cr}^{inletNa}$ was set at 0.1 wt ppm, the length along the z-axis 0.3 m, and the simulation period 3,000 h. The results for temperatures of 600°C, 650°C and 700°C correspond to those for X/L of 0.75, 0.875, and 1.0, respectively. X/L is the X to L ratio, where L is the fuel column length, and X is the distance from the bottom of fuel column. The calculation results clearly showed that the surface Cr concentration decreased with increasing flow velocity, and saturated at high flow velocities. Figure 12 shows the Cr concentration profiles in the R-direction at 650°C at the axial position (X/L=0.875), which indicates that increasing the flow velocity lowers the surface Cr concentration, thus promoting the Cr dissolution. The critical flow velocity for saturation was roughly 1 m/sec according to this calculation. This calculation result is consistent with our general knowledge on sodium corrosion, [13, 20] indicating that Na corrosion is enhanced by increasing flow velocity and that it saturates at a critical velocity. Figure 13 shows the Cr concentration profiles in the R-direction including liquid sodium part at 650°C, derived by the calculations with sodium bulk flow velocities of 0.1, 1 and 10m/sec. It can be clearly seen that increasing sodium bulk flow velocity reduces the thickness of boundary layer, thus lowering the Cr concentration at the sodium side of interface (C(1)’) to keep the mass balance at the interface, i.e. correspondence of J1(2) with J2. With increasing sodium flow velocity, C(1)’ converges on the Cr concentration in sodium bulk flow (C(0)’), and the Cr concentration at cladding surface (C(1)) converges on a Cr concentration in equilibrium with Cr in the sodium bulk flow. Therefore, in the high flow velocity range, the boundary layer becomes negligible and the flow velocity effect decreases in the calculation.

3.3 Calculation of the effects of Cr concentration in liquid Na

Figure 14 shows the calculated surface Cr concentrations for several values for $C_{Cr}^{inletNa}$. The calculated results show that a very small change in Cr concentration in liquid sodium, under 1 wt ppm, produces a pronounced effect on the threshold temperature for Cr dissolution; the threshold temperature markedly increases with a small increase in Cr concentration in sodium.

3.4 Calculation of downstream effects

Corrosion in a liquid metal loop with a thermal gradient is often mitigated in the downstream due to higher concentration of dissolved element in liquid metal compared with that in the upstream. This phenomena is generally called the downstream effect [13, 17]. According to the above calculation results (i.e., the effects of Cr concentration in liquid sodium), the possibility may exist that the downstream effects have a significant effect on Cr dissolution behavior in fuel cladding tubes. The downstream effects are possibly influenced by the fuel column length and the temperature gradient in the z-direction: the longer the fuel column, the more pronounced the downstream effect, which is due to increasing Cr dissolved into liquid sodium; the smaller the axial temperature gradient, the more pronounced the downstream effect, which is due to a smaller change in Cr solubility in liquid sodium along the z-axis. In the BOR-60 fuel pin irradiation test of 9Cr-ODS steel, the fuel column length was set at 0.3 m, which is significantly smaller than the ordinary fuel column length of fast reactor fuel. To study the possibility that this short fuel column length enhanced Cr dissolution by suppressing the downstream effects, calculations were carried out for two different fuel column lengths, 0.3 m and 1.0 m. Figure 15 shows the calculated results. The Cr concentration in liquid sodium was indeed higher for 1.0 m than 0.3 m in the fuel column length; however, the absolute value of the difference was quite small. As a result, there was no significant difference between the surface Cr concentrations calculated with the two different fuel column lengths. Therefore, it was concluded that the choice of 0.3 m fuel column length in the BOR-60 irradiation test did not significantly affect the Cr dissolution behavior of 9Cr-ODS steels. No significant downstream effects appear to take place in the SFR fuel cladding tube where the length is significantly shorter than that of sodium loop of SFR plant and the axial temperature gradient is quite large.

3.5 Comparison between measured and calculated results

The calculation results are overlaid with the measured data of BOR-60 fuel pin irradiation test in Figure 16. Both lines that show the results calculated for $\mathrm{C}_{Cr}^{inletNa}$ of 0.07 wt ppm agree roughly with the measured data, while the results calculated for $\mathrm{C}_{Cr}^{inletNa}$ of 0.01 wt ppm show disagreement with the measured data. In Figure 16, Cr dissolution calculation in 12Cr-ODS steel was conducted with the fuel column length of 0.3 m, while the fuel pin irradiation tests of 12Cr-ODS steels were carried out with a fuel column length of 0.45 m. As discussed above (i.e., the calculation of downstream effects), there is no apparent effect of the fuel column length on the calculation results; therefore, the calculation result with 0.3 m fuel column length should coincide with that with 0.45 m fuel column length. It should be noted that the cladding surface Cr concentrations calculated for 9Cr- and 12Cr-ODS steels converged approximately to a unique value (i.e., 5 wt%Cr) even though the initial Cr concentrations in both steels are quite different from each other. This result was consistent with the BOR-60 irradiation test result, and suggests that the chemical potential of Cr is a dominant parameter for cladding tube-liquid sodium interface reaction. For this reason, the surface Cr concentration should be lowered to a concentration to achieve continuity in Cr chemical potential at the interface (i.e. $\mu_{Cr}^{L} = \mu_{Cr}^{BCC}$), as schematically shown in Figure 1.

An important result in this study is that Cr dissolution was significantly influenced by a small change in Cr concentration in liquid sodium in the model calculation. This result indicates that ascertainment and control of Cr concentration in sodium coolant is essential for the prediction and management of Cr dissolution behavior in SFR cores. E. Yoshida conducted a flowing sodium corrosion test of 13-14Cr-ODS steels at 700°C using out-of-pile sodium loop equipment, and indicated the occurrence of Cr depletion and Ni enrichment at the ODS steel surface which was in contact with flowing sodium [14]. The surface Cr concentrations converged to 7-9 wt% [14], which is higher than those observed in the BOR-60 fuel pin irradiation test (roughly 5 wt%) even though the test temperature was higher in the out-of-piles test (700 °C) than in the BOR-60 irradiation test (665 °C). From the discussions based on the calculations in this study, the chemical potentials (concentrations) of Cr and Ni were considered to be higher in the out-of-piles test than in the BOR-60 irradiation test due to differences in the two sets of test equipment, including material compositions and temperature distributions in components.

The thickness of the Cr dissolution layer in this calculation was consistent with the measured data seen in Figure 16. The diffusion length of Cr was calculated for 15,000 h at 650 °C with two different Cr diffusion coefficients of ODS steel (D_{Cr}). The value of L1 was calculated by substituting the Cr diffusion coefficient in BCC-Fe [27] for D_{Cr}; in the L2 calculation, Ni diffusion coefficient in ODS steel [14] was substituted for D_{Cr} as with the calculation of Figure 16.

$$\mathrm{L1} = \sqrt{2 \cdot \mathrm{D} \cdot \mathrm{t}} = 18\ \mu\mathrm{m}$$

$$\mathrm{L2} = \sqrt{2 \cdot \mathrm{D} \cdot \mathrm{t}} = 74\ \mu\mathrm{m}$$

Since L1 is significantly shorter than L2, the selection of Cr diffusion coefficient in this calculation is thought to be appropriate. As for the Cr diffusion coefficient in ODS steels, experimental data is not yet available. An important task in the future is experimental measurement of the Cr diffusion coefficient in ODS steels for verification and validation of the calculation results. Diffusion couple experiments of ODS steel / BCC-Cr are on-going at high temperatures.

4. Summary

This study systematically and numerically evaluated Cr dissolution behavior using a model calculation. The model calculation results were compared with the data measured in a BOR-60 irradiation test and the validity of model calculation was discussed.

1) A calculation model was constructed to systematically study the effects of environmental conditions (i.e. Cr concentration in sodium, test temperature, axial temperature gradient of fuel pin, and sodium flow velocity) on Cr dissolution behavior.
2) Cr dissolution was largely influenced by a small change in Cr concentration (i.e. the chemical potential of Cr) in liquid sodium in the model calculation. Cr concentration in sodium coolant, therefore, should be noted as a critical parameter for the prediction and management of Cr dissolution behavior in SFR cores.
3) In the model calculation, the fuel column length did not show an impact on the dissolution behavior. No significant downstream effects appear to take place in the SFR fuel cladding tube where the length is much shorter than that of a sodium loop of SFR plants and the axial temperature gradient is quite large.
4) The calculated profile of Cr concentration along the wall-thickness direction was consistent with the measured data in BOR-60 irradiation test when the Cr concentration in inlet sodium bulk flow was set at 0.07 wt ppm in the calculation. Both the experimental measurement and the model calculation indicated that the cladding surface Cr concentrations in 9Cr- and 12Cr-ODS steels converged approximately to a unique value (i.e., 5 wt%Cr) even though the initial Cr concentrations in both steels are quite different from each other.

Appendix (Equation for correlation between boundary layer thickness and bulk flow velocity)

The Sherwood number (Sh_i) of solute element i is defined by:

$$Sh_i = d/_{\delta} \tag{A.1}$$

where d represents the hydraulic diameter, and δ the thickness of boundary layer. The Sherwood number is known to correlate with the Reynolds number (Re) and the Schmidt number (Sc) [18, 30]:

$$Sh_i = a \cdot Re^b \cdot Sc_i^c \tag{A.2}$$

Berger and Hsu experimentally evaluated the values of a, b and c as 0.0165, 0.860, 0.33, respectively [18, 30]. The Reynolds number and the Schmidt number are defined by:

$$Re = d \cdot U/_{\nu} \tag{A.3}$$

$$Sc_i = \nu/_{D_i'} \tag{A.4}$$

U represents the bulk flow rate, ν the kinematic viscosity of liquid, and D'_i the diffusion coefficient of solute element i in the liquid. By combining the equations from (A.1) to (A.4), the thickness of boundary layer can be expressed by:

$$\delta = \frac{d}{0.0165} \cdot \left(\frac{d \cdot U}{\nu}\right)^{-0.86} \cdot \left(\frac{\nu}{D_i'}\right)^{-0.33} \tag{A.5}$$

References

[1] S. Ukai, M. Fujiwara, J. Nucl. Mater. 307–311 (2002) 749–757.

[2] T. Kaito, S. Ohtsuka, M. Inoue, Progress in the R&D on oxide dispersion strengthened and precipitation hardened ferritic steels for sodium cooled fast breeder reactor fuels, in: Proc. GLOBAL 2007, Boise, Idaho, September 9-13, 2007, pp.37–42 (CD-ROM).

[3] S. Ohtsuka, T. Kaito, T. Tanno, Y. Yano, S. Koyama, K. Tanaka, J. Nucl. Mater. 442 (2013) S89–S94.

[4] T. Asayama, S. Ohtsuka, Development of core and structural materials for fast reactors, in: Proc. of International Conference on Fast Reactors and Related Fuel Cycles (FR17), Yekaterinburg, Russian Federation, June 26 – 29, 2017, IAEA-CN245-077.

[5] P. Dubuisson, Y. de Carlan, V. Garat, M. Blat, J. Nucl. Mater. 428 (2012) 6–12.

[6] D. T. Hoelzer, K. A. Unocic, M. A. Sokolov, T. S. Byun, J. Nucl. Mater. 471 (2016) 251-265.

[7] A. Das, H.W. Viehrig, F. Bergner, C. Heintze, E. Altstadt, J. Hoffmann, J. Nucl. Mater. 491 (2017) 83-93.

[8] D. Kumar, U. Prakash, V.V. Dabhade, K. Laha, T. Sakthivel, J. Nucl. Mater. 488 (2017) 75-82.

[9] J. H. Kim, T. S. Byun, J. H. Lee, J. Y. Min, S. W. Kim, C. H. Park, B. H. Lee, J. Nucl. Mater. 449 (2014) 300–307.

[9] H. Dong, L. Yu, Y. Liu, C. Liu, H. Li, J. Wu, J. Alloys Comp. 702 (2017) 538-545.

[10] N. H. Oono, S. Ukai, S. Hayashi, S. Ohtsuka, T. Kaito, A. Kimura, T. Torimaru, K. Sakamoto, J. Nucl. Mater. 493 (2017) 180-188.

[11] A. Kimura, R. Kasada, N. Iwata, H. Kishimoto, C. H. Zhang, J. Isselin, P. Dou, J. H. Lee, N. Muthukumar, T. Okuda, M. Inoue, S. Ukai, S. Ohnuki, T. Fujisawa, F. Abe, J. Nucl. Mater. 417 (2011) 176–179.

[12] M. Ichimiya, T. Mizuno and S. Kotake, Nucl. Eng. Technol. 39(3) (2007) 171-186.

[13] H. U. Borgstedt and C. K. Mathews, Applied chemistry of the alkali metals, Plenum Press, New York and London, 1987.

[14] E. Yoshida, S. Kato, J. Nucl. Mater. 329–333 (2004)1393–1397.

[15] T. Kaito, Y. Yano, S. Ohtsuka, M. Inoue, K. Tanaka, A. E. Fedoseev, A. V. Povstyanko, A. Novoselov, J. Nucl. Sci. Technol. 50(4) (2013) 387–399.

[16] T. Furukawa, S. Kato, E. Yoshida, J. Nucl. Mater. 392 (2009) 249–254.

[17] L. Brissonneau, J. Nucl. Mater. 423 (2012) 67–78.

[18] J. Zhang, P. Hosemann, S. Maloy, J. Nucl. Mater. 404 (2010) 82-96.

[19] J. Zhang, T. F. Marcille, and R. Kapernick, Corrosion 64 (7) (2008) 563-573.

[20] P. Roy and M. K. Schad, J. Nucl. Mater. 47 (1973) 129-131.

[21] D. A. Porter and K. E. Easterling, Phase Transformations in Metals and Alloys, Stanley

Thornes Publishers Ltd., Cheltenham, 2000.

[22] A. T. Dinsdale, Calphad 15(4) (1991) 317-425.

[23] J. O. Andersson and Bo Sundman, Calphad 11(1) (1987) 83-92.

[24] R. M. Singer, A. H. Fleitman, J.R. Weeks, and H. S. Isaacs, in: Corrosion by Liquid Metals (J. E. Draley and J. R. Weeks, Eds.), Plenum Press, New York, 1970, pp.561-576.

[25] C. W. Bale, E. Bélisle, P. Chartrand, S. A. Decterov, G. Eriksson, A. E. Gheribi, K. Hack, I.-H. Jung, Y.-B. Kang, J. Melançon, A. D. Pelton, S. Petersen, C. Robelin, J. Sangster, P. Spencer, M-A. VanEnde, CALPHAD 54 (2016) 35-53.

[26] T. Iida, Yousetsu-Gakkai-shi 63(2) (1994) 70-75 (in Japanese).

[27] Japan Institute of Metals: Metals data book, Maruzen Press, Tokyo, 2004, pp. 21–22 (in Japanese).

[28] O. J. Foust, Sodium-NaK Engineering Handbook Vol. I Sodium Chemistry and Physical Properties, Gordon and Breach Science Publishers. Inc., 1972.

[29] M. Iijima, K. Hara, T. Hatakenaka, S. Suzuki, K. Imai, T. Horigome, M. Suzuki, K. Ozawa, Y. Yamashita, Purity control results of coolant sodium and Argon gas in Joyo; Data collections of purity control (1975-1987), PNC TN9450 88-005 (1988) (in Japanese).

[30] F. Berger, K. F. F. L. Hau, Int. J. Heat Mass Trans. 20 (1977) 1185-1194.

[Table and figure captions]

Table 1 Diffusion coefficients adopted in this calculation.

Table 2 Physical properties of liquid sodium adopted as input parameters for this calculation.

Figure 1 Schematic view of Cr dissolution model adopted in this study.

Figure 2 Schematic view of geometric mesh partitioning for Cr dissolution calculation.

Figure 3 Schematic view of the cross-sectional area of sodium flowing channel (S) and circumferential length in contact with flowing sodium, (a+b), which were assumed for calculation.

Figure 4 Flow chart for model calculation of Cr dissolution.

Figure 5 Schematic view of one-dimensional Cr diffusion calculation model.

Figure 6 Comparison of Cr solubility data measured in liquid sodium [13, 24] and those obtained by phase equilibrium calculation.

Figure 7 Calculated Cr concentrations in BCC Fe-Cr and liquid Na-Cr where the Cr chemical potentials in both phases are identical.

Figure 8 Diffusion coefficient data of Cr and Ni in BCC-Fe [27] and those of Ni in ODS steel [14].

Figure 9 Axial (Z-direction) temperature profiles in cladding tubes for two different fuel column lengths adopted in the calculation: 0.3 m and 1.0 m.

Figure 10 WDX line analysis results of 9Cr- and 12Cr-ODS steel cladding tubes in transverse-section after the second irradiation test at BOR-60 (at the top of fuel column; time-averaged irradiation temperature: 665 °C, test duration : 13,570 h, neutron dose: 24 dpa).

Figure 11 Calculated Cr concentrations at outer surface of cladding tube as a function of sodium bulk flow velocity. Cr concentration in inlet sodium coolant ($\mathrm{C}_{Cr}^{inletNa}$) was set at 0.1 wt ppm for this calculation.

Figure 12 Calculated Cr concentration profiles along the R-direction (wall thickness direction) at 650 °C at the axial position (X/L = 0.875). Cr concentration in inlet sodium coolant ($\mathrm{C}_{Cr}^{inletNa}$) was set at 0.1 wt ppm for this calculation.

Figure 13 Calculated Cr concentration profiles along the R-direction including liquid sodium part at 650°C at the axial position (X/L=0.875). Cr concentration in inlet sodium coolant ($\mathrm{C}_{Cr}^{inletNa}$) was set at 0.1 wt ppm, and simulation time was 3,000h for this calculation.

Figure 14 Calculated surface Cr concentrations for several values for Cr concentration in inlet sodium coolant ($\mathrm{C}_{Cr}^{inletNa}$).

Figure 15 Calculated results of Cr concentration at cladding tube surface and Cr concentration in sodium bulk flow as a function of temperature. Correspondence of temperature with axial position in both cases (L=1.0 m, 0.3 m) are indicated in Figure 9.

Figure 16 Comparison of the calculated Cr concentration profiles with data measured by fuel pin irradiation test in BOR-60 (at the top of fuel column of the second irradiation test pin, Figure 10).

Table 1 Diffusion coefficients adopted in this calculation.

Medium	Diffusion coefficient of Cr *		Remarks	Ref.
	D_0 (m^2/sec)	Q (J/mol)		
Liquid sodium	8.6×10^{-8}	9.29×10^{3}	Measured self-diffusion coefficient of Cr in liquid sodium (103-284 °C)	[26]
ODS steel	9.37×10^{-9}	1.46×10^{5}	Measured diffusion coefficient of Ni in ODS steels	[14]

$* \ \mathrm{D} = \mathrm{D}_0 \times \exp(-Q/RT)$

Table 2 Physical properties of liquid sodium adopted as input parameters for this calculation.

Item	Physical property equation for liquid sodium	Ref.
Density (g/m^3)	$\rho_{Na} = 950100 - 229.76 \times T - 0.0146 \times T^2$ $+5.638 \times 10^{-6} \times T^3$	[28]
Kinematic viscosity (m^2/sec)	$\nu_{Na} = 0.0851 \cdot \rho_{Na}{}^{-2/3} \cdot exp(1040 \cdot \rho_{Na}/(T - 273.15))$	[28]

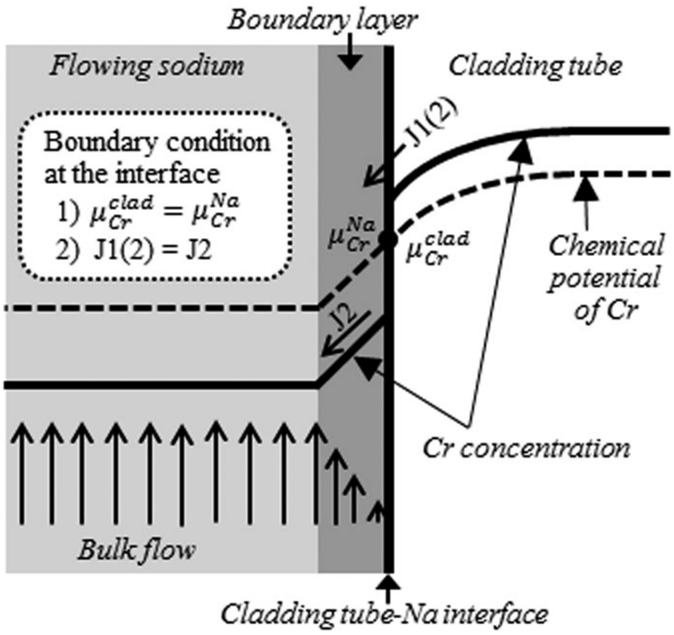

Figure 1 Schematic view of Cr dissolution model adopted in this study.

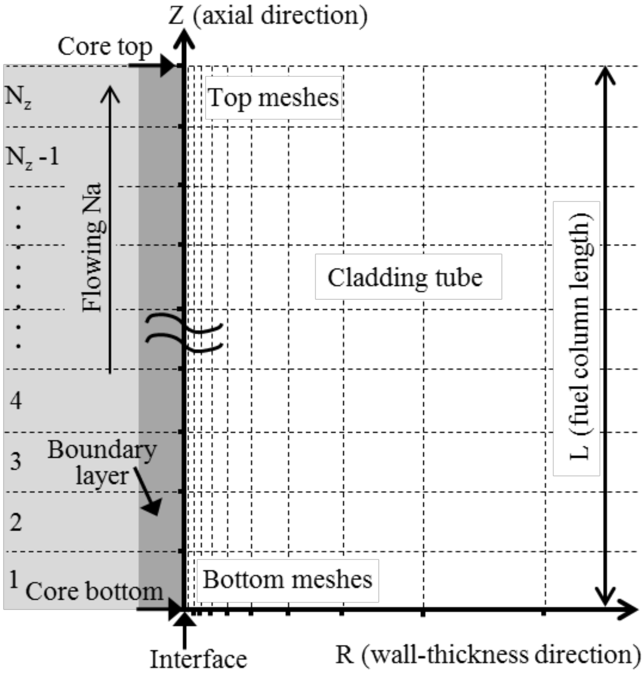

Figure 2 Schematic view of geometric mesh partitioning for Cr dissolution calculation.

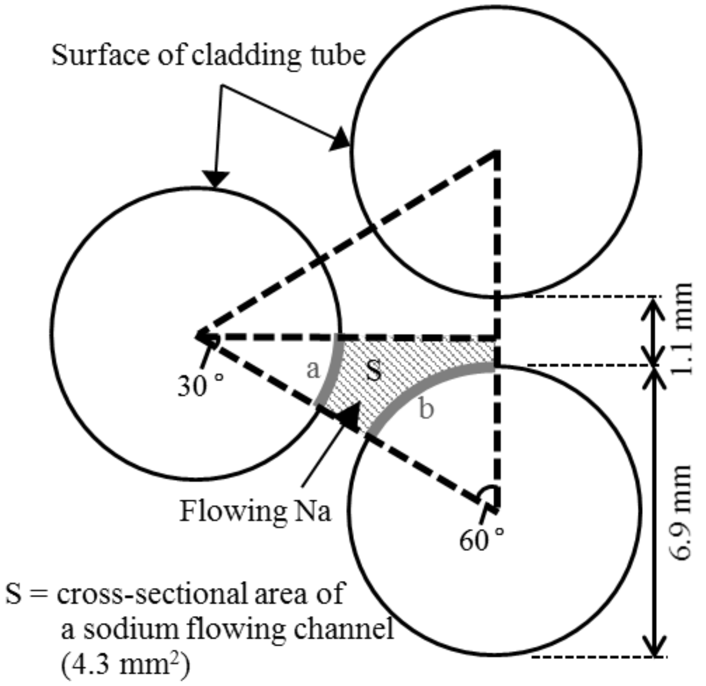

S = cross-sectional area of a sodium flowing channel ($4.3\ \mathrm{mm}^2$)

a+b = circumferential length in contact with flowing sodium (5.4 mm)

Hydraulic diameter (d) = $4 \times S/(a+b) = 3.2$ mm

Figure 3 Schematic view of the cross-sectional area of sodium flowing channel (S) and circumferential length in contact with flowing sodium, (a+b), which were assumed for calculation.

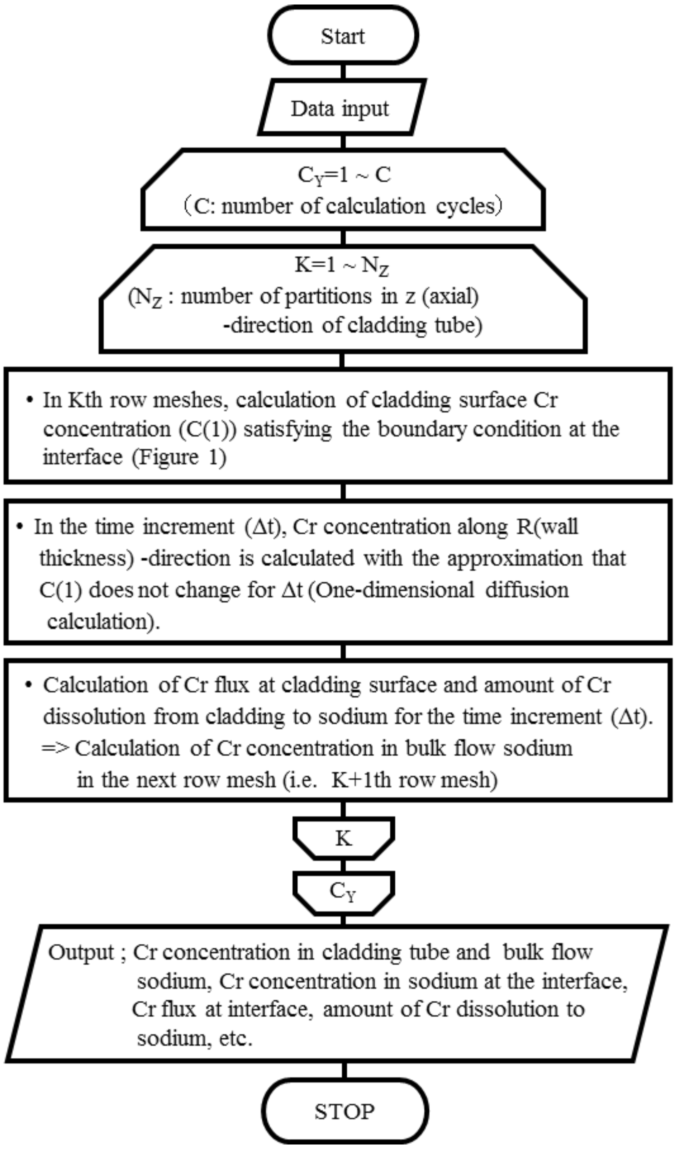

Figure 4　Flow chart for model calculation of Cr dissolution.

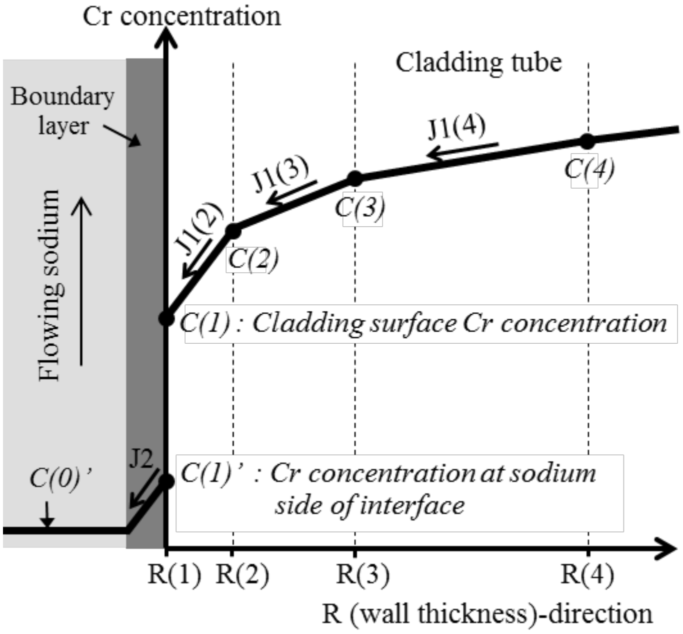

Figure 5 Schematic view of one-dimensional Cr diffusion calculation model.

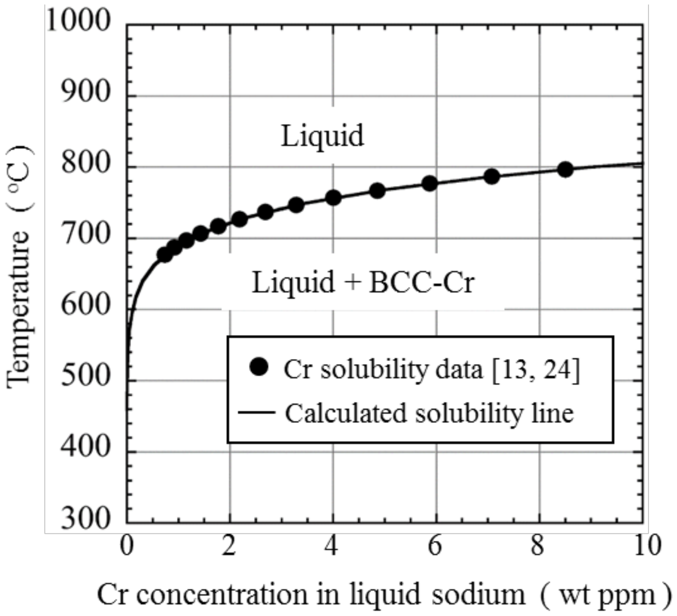

Figure 6 Comparison of Cr solubility data measured in liquid sodium [13, 24] and those obtained by phase equilibrium calculation.

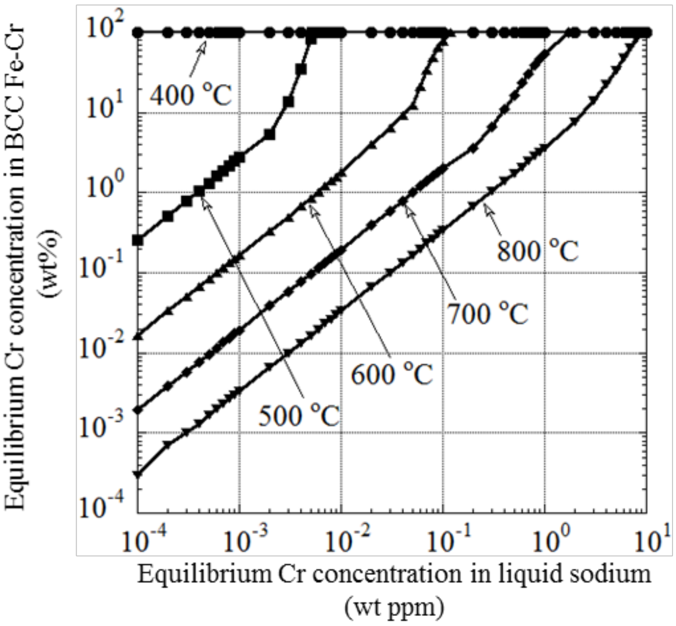

Figure 7 Calculated Cr concentrations in BCC Fe-Cr and liquid Na-Cr where the Cr chemical potentials in both phases are identical.

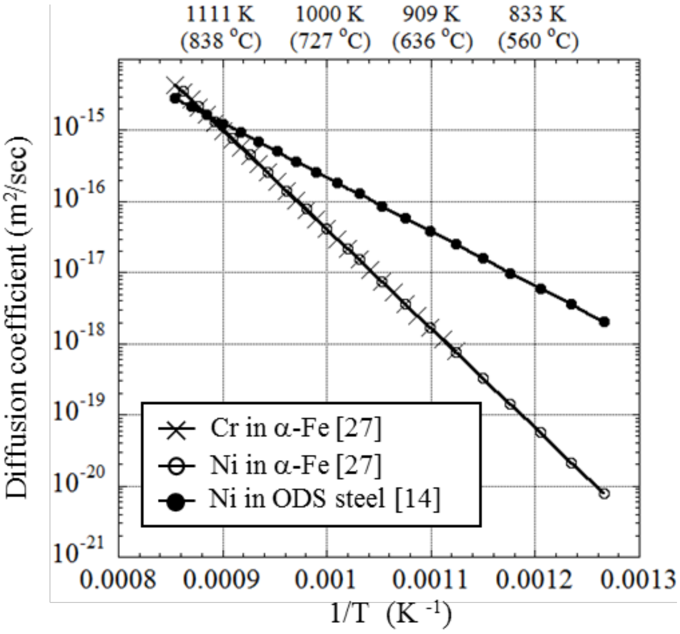

Figure 8 Diffusion coefficient data of Cr and Ni in BCC-Fe [27] and those of Ni in ODS steel [14].

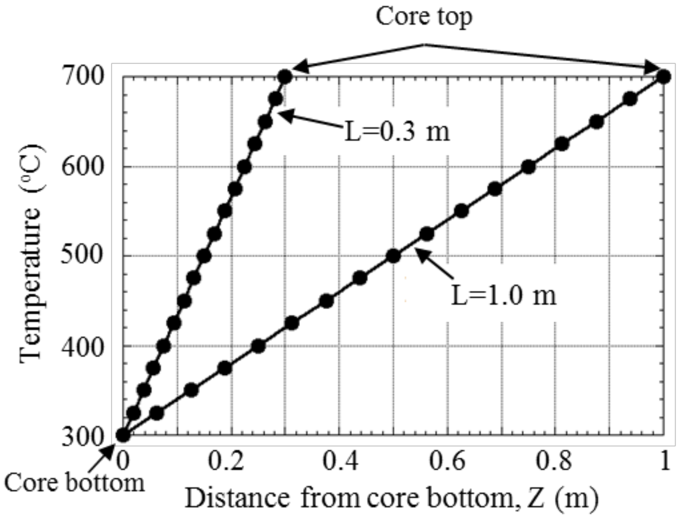

Figure 9 Axial (Z-direction) temperature profiles in cladding tubes for two different fuel column lengths adopted in the calculation: 0.3 m and 1.0 m.

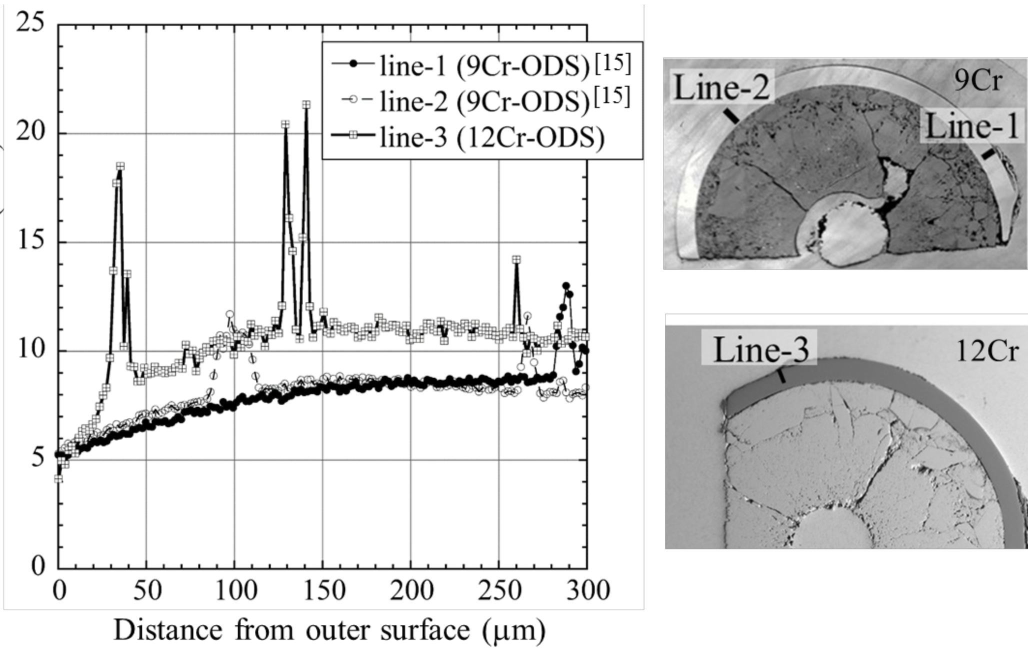

Figure 10 WDX line analysis results of 9Cr- and 12Cr-ODS steel cladding tubes in transverse-section after the second irradiation test at BOR-60 (at the top of fuel column; time-averaged irradiation temperature: 665 °C, test duration : 13,570 h, neutron dose: 24 dpa).

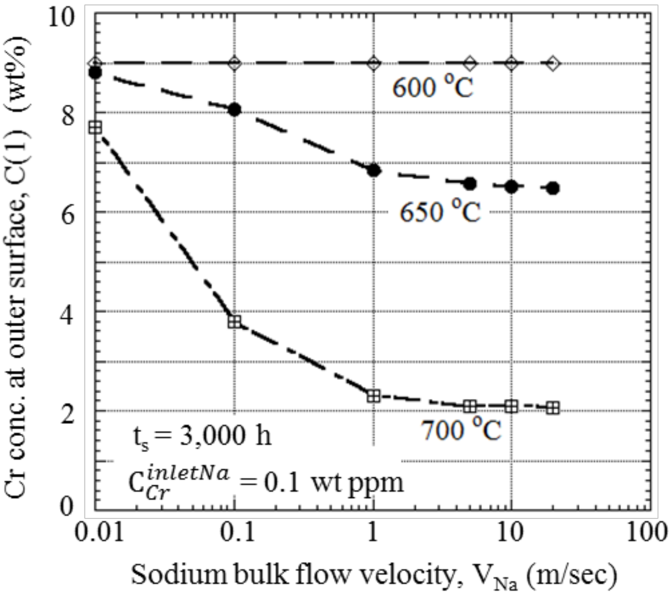

Figure 11 Calculated Cr concentrations at outer surface of cladding tube as a function of sodium bulk flow velocity. Cr concentration in inlet sodium coolant ($C_{Cr}^{inletNa}$) was set at 0.1 wt ppm for this calculation.

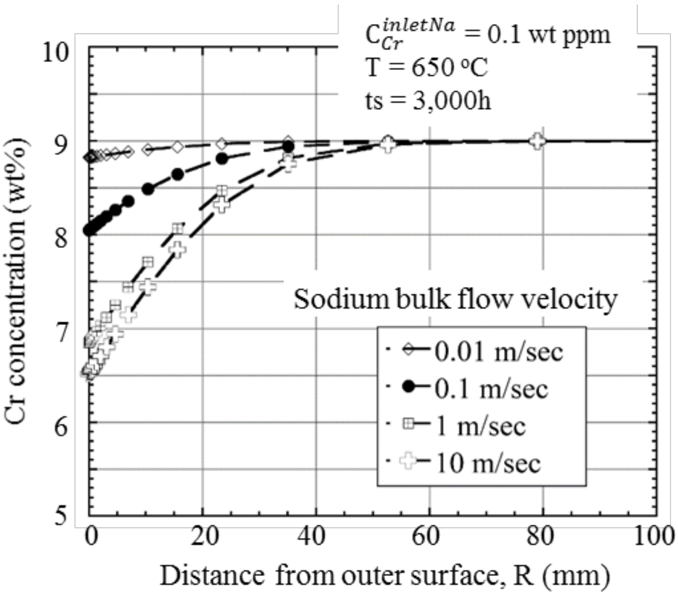

Figure 12 Calculated Cr concentration profiles along the R-direction (wall thickness direction) at 650°C at the axial position (X/L=0.875). Cr concentration in inlet sodium coolant ($C_{Cr}^{inletNa}$) was set at 0.1 wt ppm for this calculation.

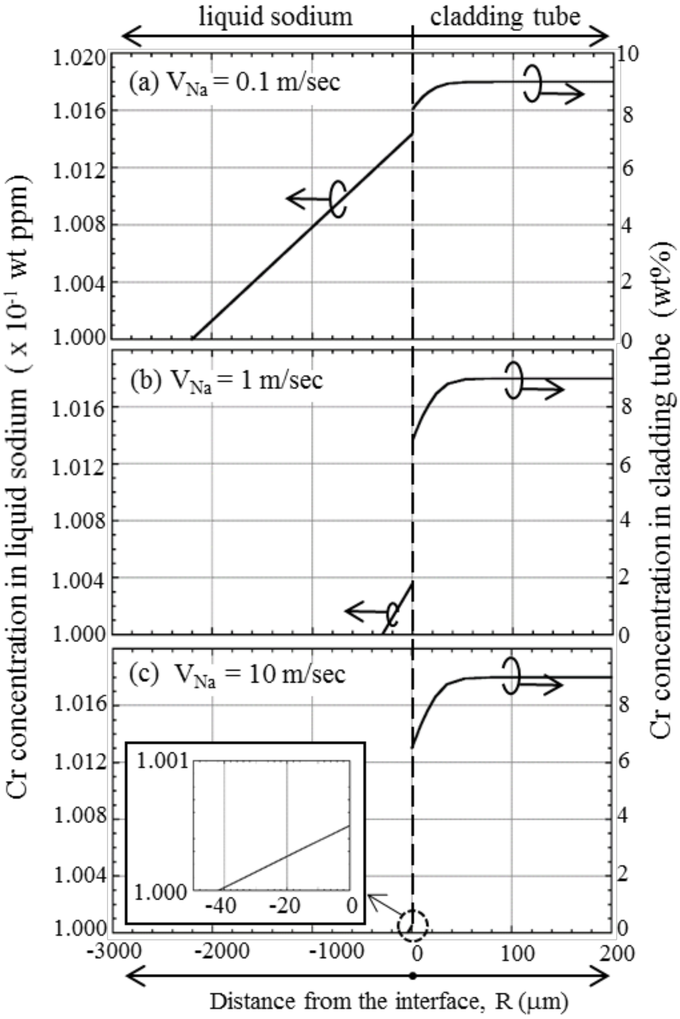

Figure 13 Calculated Cr concentration profiles along the R-direction including liquid sodium part at 650°C at the axial position (X/L=0.875). Cr concentration in inlet sodium coolant ($C_{Cr}^{inletNa}$) was set at 0.1 wt ppm, and simulation time was 3,000h for this calculation.

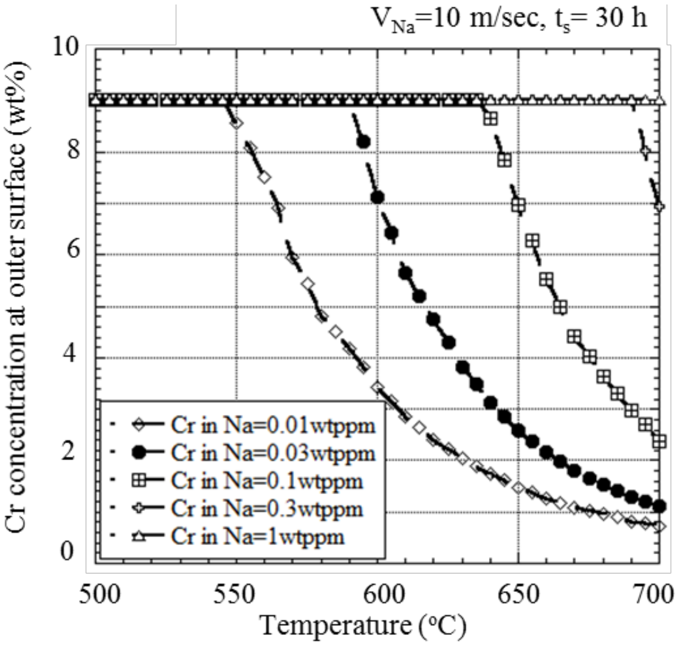

Figure 14 Calculated surface Cr concentrations for several values for Cr concentration in inlet sodium coolant ($C_{Cr}^{inletNa}$).

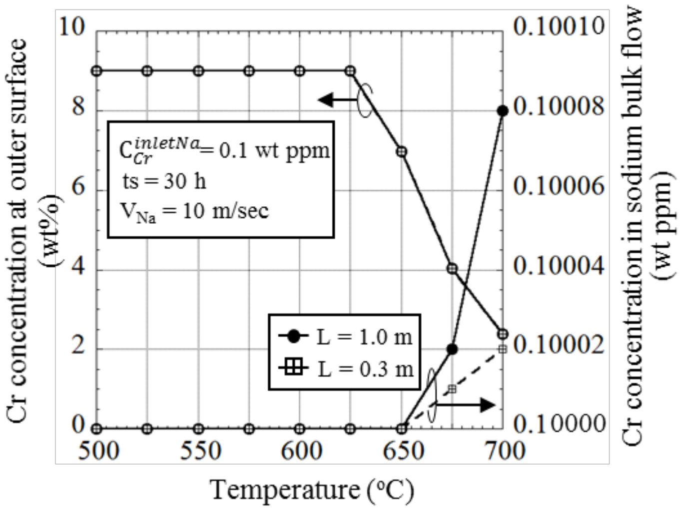

Figure 15 Calculated results of Cr concentration at cladding tube surface and Cr concentration in sodium bulk flow as a function of temperature. Correspondence of temperature with axial position in both cases (L=1.0 m, 0.3 m) are indicated in Figure 9.

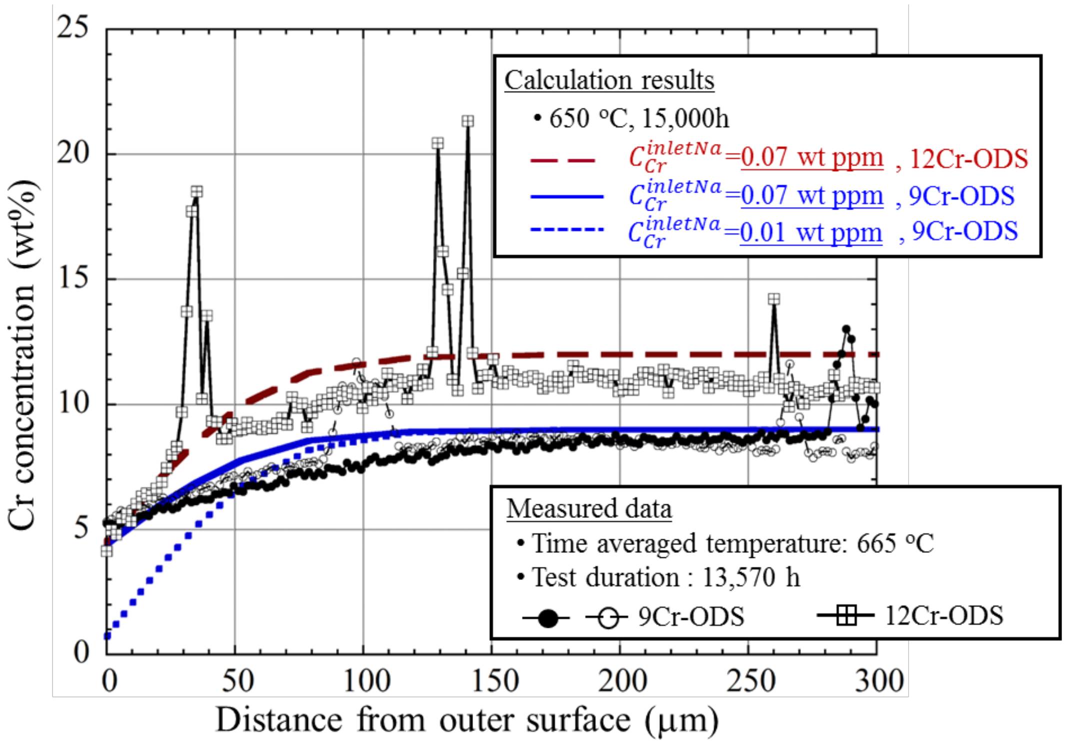

Figure 16 Comparison of the calculated Cr concentration profiles with data measured by fuel pin irradiation test in BOR-60 (at the top of fuel column of the second irradiation test pin, Figure 10).